

Transformation of twin-peak electromagnetically induced transparency to twin-peak electromagnetically induced absorption based on magnetic dipole and dielectric resonator

Yu-jing Yin, You Lv, Didi Zhu & Hai-Feng Zhang

To cite this article: Yu-jing Yin, You Lv, Didi Zhu & Hai-Feng Zhang (2023): Transformation of twin-peak electromagnetically induced transparency to twin-peak electromagnetically induced absorption based on magnetic dipole and dielectric resonator, Waves in Random and Complex Media, DOI: [10.1080/17455030.2023.2239374](https://doi.org/10.1080/17455030.2023.2239374)

To link to this article: <https://doi.org/10.1080/17455030.2023.2239374>



Published online: 27 Jul 2023.



Submit your article to this journal [↗](#)



View related articles [↗](#)



View Crossmark data [↗](#)



Transformation of twin-peak electromagnetically induced transparency to twin-peak electromagnetically induced absorption based on magnetic dipole and dielectric resonator

Yu-jing Yin^a, You Lv^b, Didi Zhu^b and Hai-Feng Zhang^b

^aCollege of Communications and Information Engineering, Nanjing University of Posts and Telecommunications, Nanjing, People's Republic of China; ^bCollege of Electronic and Optical Engineering & College of Flexible Electronics (Future Technology), Nanjing University of Posts and Telecommunications, Nanjing, People's Republic of China

ABSTRACT

This paper puts forward the transmission from twin-peak electromagnetically induced transparency (EIT) to twin-peak electromagnetically induced absorption (EIA), while it is rare to see the transformation between EIT and EIA in metastructure (MS) in one device in previous articles. With the incidence of TE waves, two transparent windows are generated, ranging from 0.382 THz to 0.986 THz which are separated by 0.604 THz, when the conductivity of vanadium dioxide (VO₂) is set to 10 S/m. Two peaks reach 0.864 and 0.934, respectively, accompanied by the largest group delays of the two peaks being 7.55 and 4.54 ps. In addition, VO₂ blocks in the metallic state will affect interference paths between energy levels, contributing to the formation of EIA, then maintaining a common absorption of 0.607 at 0.429 THz and 0.904 at 0.678 THz. Under the combined action of the dielectric resonator and metal resonator, the conversion from bimodal EIT to bimodal EIA is hardly been researched, at the same time, the adoption of the circuit model and the four-level theory proves the rationality of the model. The transformation from EIT to EIA is aroused by changing the state of VO₂, promising broad prospects in multifunctional devices.

ARTICLE HISTORY


Received 7 January 2023
Accepted 17 July 2023


KEYWORDS

Metastructure; twin peaks; electromagnetically induced transparency; electromagnetically induced absorption; vanadium dioxide

1. Introduction

Electromagnetically induced transparency (EIT) has been studied as early as the last century, which refers to a phenomenon of destructive interference first discovered in three-level atomic systems, exhibiting a steep transmission peak with a restricted band [1,2]. The classic EIT phenomenon arises from bright mode coupling with dark one in the near-field [3,4], there are subsequent articles that have proposed bright-bright modes coupling, as proposed by Yahiaoui et al. [5], based on the weak hybridization of the two resonators. In 2016, Han et al. proposed Tunable EIT in coupled three-dimensional split-ring-resonator metamaterials [6]. In addition, the EIT model is frequently used to generate an electric dipole

CONTACT Hai-Feng Zhang  hanlor@njupt.edu.cn

 Supplemental data for this article can be accessed here. <https://doi.org/10.1080/17455030.2023.2239374>

response linking a magnetic dipole response using metallic resonators, as demonstrated by the work by Yin et al. [7], through changing the position of gold resonators, arriving at the changes in the transmission window. It is worth mentioning that the dielectric is also put into use. Fano resonance is similar to the EIT phenomenon in three level atom systems, but it is produced in plasmon systems and often has a very high Q value [8–11]. Al-Naib et al also achieved high-Q subradiant resonance in 2012 [12], while Yang et al. exploited silicon in 2014 and achieved EIT with a high Q value that ended up at 483. More and more dielectrics are being used in the investigation of EIT thanks to the incredibly low absorption loss and coherent interaction of nearby meta-atoms [13,14]. Numerous studies also focus on broadband and multi-frequency EIT in addition to single-peak narrow-band EIT [15,16]. Zhang et al. demonstrate a polarization-independent PIT metamaterial functioning in the terahertz regime [17]. In this paper, twin-peak EIT is shaped, with the left peak formed by magnetic dipole coupling dielectric while another is generated from the coupling of two dielectric resonators. What distinguishes this work from its predecessors is the combination of the advantages of the dielectric and metal resonators and the more optimized peak values. Special electromagnetic field properties of the ring dipole created by the magnetic dipole allow for greater radiation reduction, coupling with the dielectric resonator with low absorption loss, and a higher transmission peak of EIT.

Electromagnetically induced absorption (EIA), an enhancement of the absorption resulting from atomic coherence induced by optical radiation, serves as the complementary phenomenon of EIT. EIA is first studied by Lezama et al. In 1998, [18] the theoretical condition for implementing EIA was given in that work. Additionally, Taubert et al. [19] first experimentally investigated EIA with plasmonic resonators, recognizing that altering the phase might boost the absorption effect. In the same year, a radiating dual-oscillator model was introduced by Tassin et al. [20] to depict both the absorption and the scattering properties, revealing that the transition from EIT to EIA is accomplished via increasing the dissipative loss of the dark resonator and decreasing the coupling strength. The radiation-broadened resonators are applied in his work to make up for the impossibility of reaching the phase difference in truly homogenized metastructure (MS) to achieve EIA. Besides, phase-shift modulations have been proven a wonderful approach to transforming EIT into EIA. A triple-resonator was put forward by Zhang et al., [21] the change of the difference of phase at the resonance frequency between the surface currents of three resonators leading to the shift from EIT to EIA with its near-field absorption caused by a strong magnetic response. Although research on EIA is not rare, too, few people pay attention to the auto transformation from EIT to EIA, which requires our attention. In this paper, vanadium dioxide (VO_2) is employed to promote the switch between twin-peak EIT and twin-peak EIA.

VO_2 , a well-known phase change material, is widely used in the design of MS. 68°C serves as a dividing line between the metallic and dielectric states, with this feature EIA being able to be achieved without influencing EIT in the metallic state [22]. Under these extraordinary features, VO_2 can also be applied in diverse advanced contexts, such as optical switches [23,24], modulators [25,26], thermal sensors [27,28], and so forth, has been reported. There are many more tunable materials, such as solution-lead iodide (PbI_2) [29]. In addition to temperature control materials, electronic control materials, and other multi-functional integration are also put into use [30].

This model works in the terahertz (THz) band, with interest in this band growing continuously in recent years and becoming more and more widely used in the fields of slow

light [31], signal processing [32], optical storage [33], and sensing [34,35]. In the last several years, plane resonance devices based on the principle of electromagnetic resonance attract growing attention. Besides, unique electromagnetic characteristics of MS enable its many potential applications, such as perfect stealth [36], negative refraction [37], and imaging [38]. In the long run, the development of MS is of great significance for scientific research [39].

In this work, the transmission curve stimulated by the transverse electric (TE) wave maintains two transparent windows ranging from 0.382 THz to 0.986 THz, separated by 0.604 THz, with two peaks of 0.864 and 0.934, respectively. The twin-peak EIT with two transmission peaks that apply different coupling principles possesses a wide range of applications. Besides, the largest group delays of the twin-peak EIT arrive at 7.55 and 4.54 ps, respectively, proving the slow light effect of EIT. In addition, the application of VO₂ blocks promotes the form of EIA, maintaining two absorption windows in the original EIT window, with two absorption peaks of 0.607 at 0.429 THz and 0.904 at 0.678 THz, the medium state of which has a small impact on EIT. The different states of VO₂ are integrated based on EIT and EIA, respectively, this switchable metasurface between twin-peak EIT and twin-peak EIA might promise a novel way to the electromagnetic induction switch with wide prospects in radomes, optical retarders, polarization detections, and other information front-end processors.

Compared with Ref. [40], the model in this paper is easier to adjust and enjoys better phenomenon. Additionally, the adoption of the circuit model and the atomic energy level theory enables readers to understand better. In comparison with [41], different from the visible and near-infrared wavelengths, the band studied in this paper is THz. Moreover, the theory of EIA differs from perfect absorption

Fabrication challenges for multiple-layer structure cannot be ignored, however, since our team mainly studies the direction of electromagnetic fields and microwaves and focus on theory, we can only display the general production process. The molecular beam epitaxy method is applied to lay silicon on base [42], on the silicon dielectric substrate, the metal resonator pattern can be defined by photolithography, and gold can be deposited by E-beam evaporation [43], which is common in the fabrication of metal structures. Titanium dioxide (TiO₂) capacitors were fabricated on a silicon layer using E-beam evaporation, too [44]. The fabrication process of the VO₂ could be found in Refs. [45–48]. The steps of TiO₂ are repeated two times and transferred cumulatively layer by layer according to the design. It can be seen in the work of the predecessors that Singh et al. experimentally verified the phenomenon that bright mode coupling dark mode could form EIT in the THz band in 2014, and Yang et al. found the phenomenon that all-dielectric resonators could form EIT in 2014 through experiment. Besides, Zhang et al. experimentally realized EIA in 2015 by using three-layer structural coupling [21,49,50].

2. Structure design

The final integrated structure and the periodic principle are displayed in detail in Figure 1. Figure 1(a) demonstrates decentralized diagrams in the direction of the z-axis. The whole structure is composed of five resonators, with the base made of quartz [51] and the middle medium partition constituted by silicon. The S-shaped resonator (SSR) fabricated of gold [52] on the bottom layer is composed of two split ring resonators with openings in the

2. Structure Design

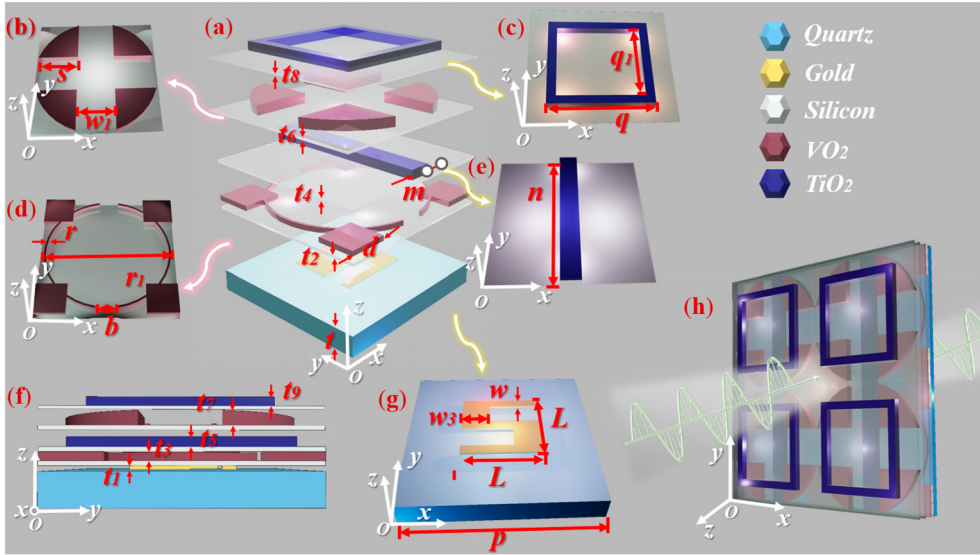


Figure 1. (a) Gives the presentation of the resonators scattering in the z -axis, (b), (c), (d), (e), and (g) respectively exhibit the separate resonator on each layer, (f) reveals the side view of the model, (h) the array of the reconfigurable electromagnetically induced system where the linearly polarized (LP) wave works as the incident wave.

Table 1. Some main parameters of the structure.

Parameter	Value (μm)	Parameter	Value (μm)	Parameter	Value (μm)
w	11	m	25	b	30
w_1	60	n	200	t	20
w_3	30	d	45	r	3
p	200	q	143	r_1	94
L	86	q_1	118		

opposite direction, detailed in Figure 1(g). The dielectric applied in the vertical rod (VR) and the square ring (SR) is titanium dioxide (TiO_2 , relative permittivity $\varepsilon_{\text{TiO}_2} = 114$, loss tangent $\tan\delta_{\text{TiO}_2} = 0.00027$) [53], as shown in Figure 1(c) and Figure 1(e). Sandwiched between the three resonators, as displayed in Figure 1(b,d), are the open ring with blocks (ORB) and four fan-shaped blocks (FFB), they use VO_2 together. The specific parameters of the design are given in Table 1.

2.1. The appearance of EIT phenomenon

The electrical vector of the TE wave is perpendicular to the incident surface, with the electric field direction along the y -axis direction of the coordinate axis, traveling along the radial of VR. With the incidence of TE wave, the three resonators can be directly excited at 0.42 THz, 0.60 THz, and 0.99 THz, and correspondingly the resonant curves are displayed in Figure 2(a–c). SSR resonated with SR and VR, respectively, producing two transparent windows. Thanks to the far distance between the resonance frequency reaching up to 0.57 THz, the resonant frequency points are far enough that the interference between SSR and SR is

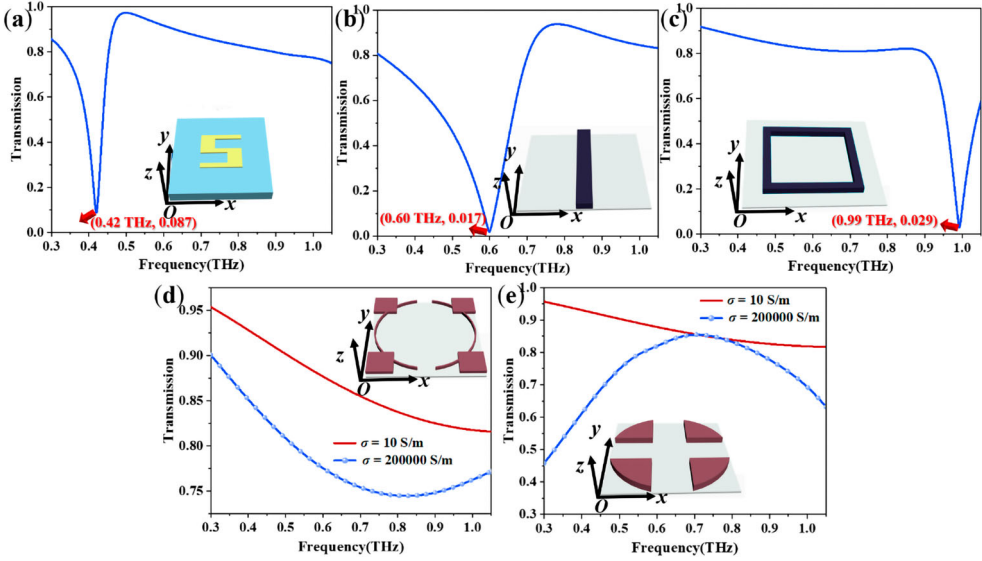


Figure 2. (a) (b), and (c) Incentive curves under the TE wave of S, VR, and SR, (d) and (e) The transmission curves of the two resonators made of VO₂ gotten under $\sigma = 10$ S/m and $\sigma = 200,000$ S/m, respectively.

weak enough to be ignored. As is exhibited in Figure 2(d,e), two resonators made of VO₂ do not participate in the formation of EIT at $\sigma = 10$ S/m. Unlike the classic structure adopting bright-mode coupling dark-mode, the two peaks in this paper all utilize bright-mode coupling bright-mode, and the EIT phenomenon is given in Figure 3. Through the comparison between the transmission curves excited separately and three zero-transmission points in the EIT curve, it becomes evident that the double transparency window is a direct consequence of spectral combinations of VR, SR, and SSR. Moreover, the work accomplished by Wang and his team [54] combined 4 dark modes which cannot be directly simulated alone, the four dark resonators couple, and then produced resonance under the electromagnetic wave. Generally speaking, the value of the quality factor (Q value) of the dark mode is larger than the bright mode, as a result of which the bright mode with a larger Q value can analog the role of the dark mode in the coupling process. The Q value can be calculated by the equation below [27]:

$$Q = f/\Delta f \quad (1)$$

where f represents the resonance frequency, Δf symbols the half-maximum bandwidth. To calculate, the Q value of the transmission peak on the left arrives at 5.6 while the other reaches 4.25.

The surface and displacement currents of the corresponding resonators when inspired separately are shown in Figure 4. Compared with the current when an interaction is exhibited in Figure 5, the surface current of SSR is largely strengthened while the displacement current of VR is weakened at the peak of the first transparent window at 0.422 THz, at which time the displacement current of SR is too weak that can be ignored. When switching to the right transparent window, it turns out that the displacement current of VR is greatly

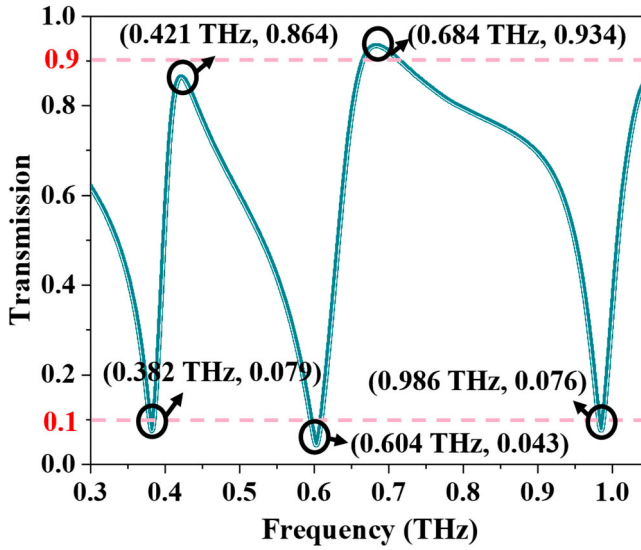


Figure 3. The simulated transmission curve of the whole model when $\sigma = 10 \text{ S/m}$.

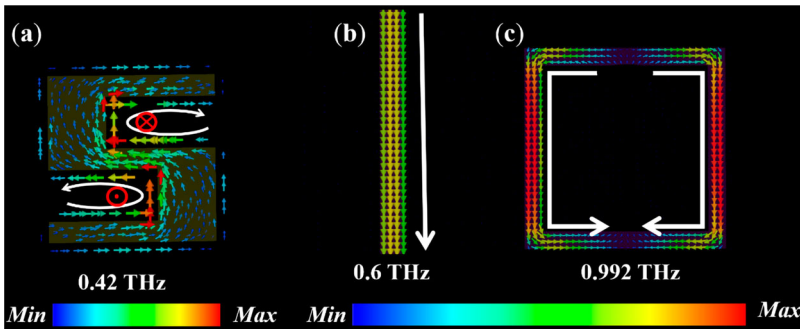


Figure 4. (a) The surface current generated when SSR is excited by TE waves alone at 0.42 THz, (b), and (c) The displacement current distributed on VR and SR when they are separately simulated at 0.6 and 0.992 THz, respectively.

enhanced at 0.684 THz, accompanied by the relative weakening displacement current compared with the separate resonance of SR. Similarly, the weak resonance of S in 0.684 THz can also be neglected. It can be captured from Figures 4 and 5 that clockwise and counter-clockwise surface current loops are displayed in the up and down parts of SSR, respectively, such magnetic moment can be gotten through the right-hand rule, as shown in Figure 6, found in the pair of surface current loops, which indicates the formation of a dipole resonance moment along the y-axis. The current direction of the current in SSR is reversed, along with the orientation of the magnetic moment, when the EIT phenomenon is generated. Then comes the reverse current of VR passing through the magnetic pole, a circular dipole response appearing, given in Figure 6. With the incidence of TE wave, VR is directly excited to generate displacement current, the coupling of SSR and VR explaining the reason for the formation of the first EIT peak.

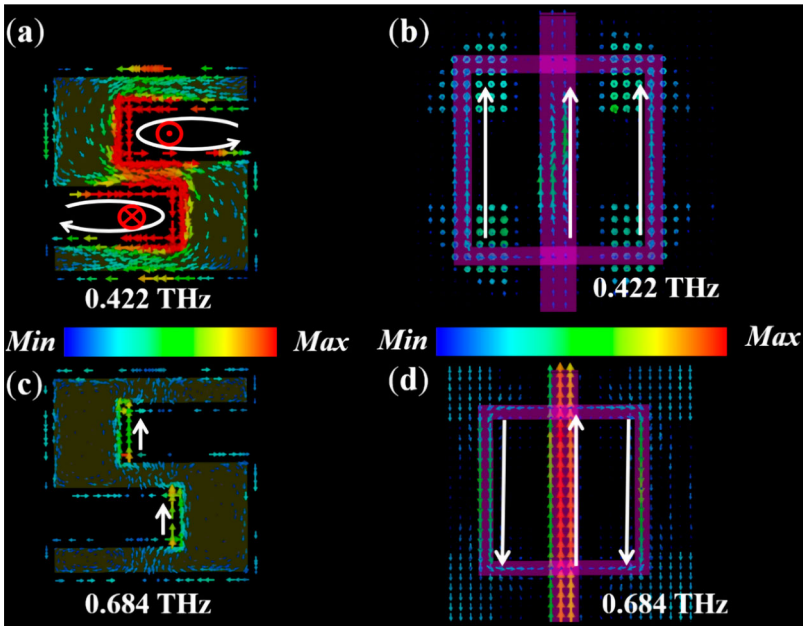


Figure 5. (a) and (c) Different current distributions of SSR on the left peak value at 0.422 THz and on the right peak value at 0.684 THz, (b) and (d) Under two transmission windows the displacement current distributions of VR and SR at 0.422 and 0.684 THz, respectively.

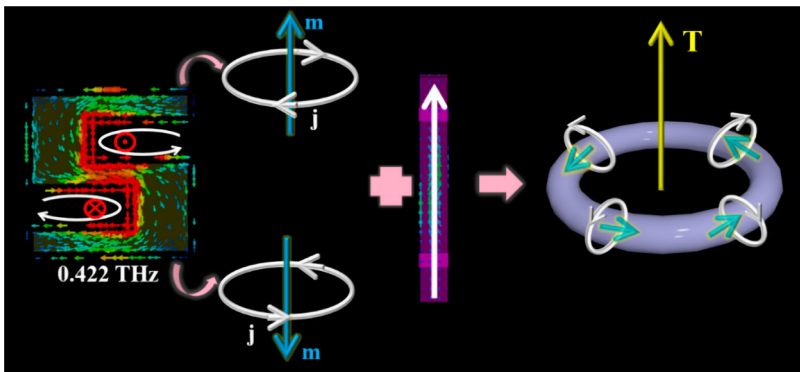


Figure 6. Schematic diagram of circular dipole response between SSR and VR.

The appearance of the right EIT window is owing to the resonance generated by VR and SR, which can be regarded as the role of an all-medium resonator. The two upper resonators are both excited to form a strong displacement current, which can be regarded as the electric dipole, then VR and SR resonating for the interaction of the displacement current. The displacement current of VR is relatively weaker compared with SR, for the larger size will reduce the coupling strength with incident plane waves. During the coupling, the direction of the displacement current of VR is reversed, leading to the electric displacement of the two resonators turning opposite in orientation. Then, VR and SR perform weak hybrid coupling, with the weakening of the surrounding electric field of the SR, causing the

emergence of the EIT window. Besides, Fano resonance is the coupling effect arising from the interaction between narrow discrete states (dark modes) and broad continuous states (bright modes) [55–57]. EIT can also be originally deemed as the Fano resonance under certain conditions [58,59]. However, the phase mutation displayed later, the coupling analysis of three bright modes and atlas of the time domain can prove the EIT phenomenon in this work.

The toroidal resonance occurs at 0.422 THz. We can get this conclusion through observing multipole decomposition. The spatial distribution of the conduction current density or displacement current density with the electromagnetic wave frequency can be used to determine the electromagnetic multipole moment of the scatterer.

The expression of the multipole moment has been displayed below in accordance with Equations (2)–(11) [60,61]:

$$P = \frac{1}{i\omega} \int J d^3r \quad (2)$$

$$M = \frac{1}{2c} \int [r \times J] d^3r \quad (3)$$

$$TO = \frac{1}{10c} \int [(r \cdot J)r - 2r^2 J] d^3r \quad (4)$$

$$Q^e_{\alpha\beta} = \frac{1}{i2\omega} \int [r_{\alpha} j_{\beta} + r_{\beta} j_{\alpha} - \frac{2}{3}(r \cdot J)] d^3r \quad (5)$$

$$Q^m_{\alpha\beta} = \frac{1}{3c} \left(\int [(r \cdot J)_{\alpha} r_{\beta}] d^3r + \{\alpha \leftrightarrow \beta\} \right) \quad (6)$$

where J , ω , and c stand for the current density, angular frequency, and speed of light, respectively, and P , M , TO , $Q^e_{\alpha\beta}$, $Q^m_{\alpha\beta}$ represent the electric dipole, magnetic dipole, toroidal dipole, electric quadrupole, and magnetic quadrupole, respectively.

$$I_p = \frac{2\omega^4}{3c^3} |P|^2 \quad (7)$$

$$I_M = \frac{2\omega^4}{3c^3} |M|^2 \quad (8)$$

$$I_{TO} = \frac{2\omega^4}{3c^3} |TO|^2 \quad (9)$$

$$I^e_Q = \frac{\omega^6}{3c^5} \sum |Q^e_{\alpha\beta}|^2 \quad (10)$$

$$I^m_Q = \frac{\omega^6}{40c^5} \sum |Q^m_{\alpha\beta}|^2 \quad (11)$$

where I_p , I_M , I_T , I^e_Q , and I^m_Q respectively, stand for the scattering strengths of electric, magnetic, toroidal, electric quadrupole, and magnetic dipoles. Figure 7 displays the EIA's scattering power at various multipoles as described in this paper.

As can be seen, the scattering power of the toroidal dipole TO within the absorption band is greater than that of the electric dipole P , magnetic dipole M , the electric quadrupole $Q^e_{\alpha\beta}$ and the magnetic quadrupole $Q^m_{\alpha\beta}$ around 0.422 THz, which suggests that it is primarily annular resonance at the first peak.

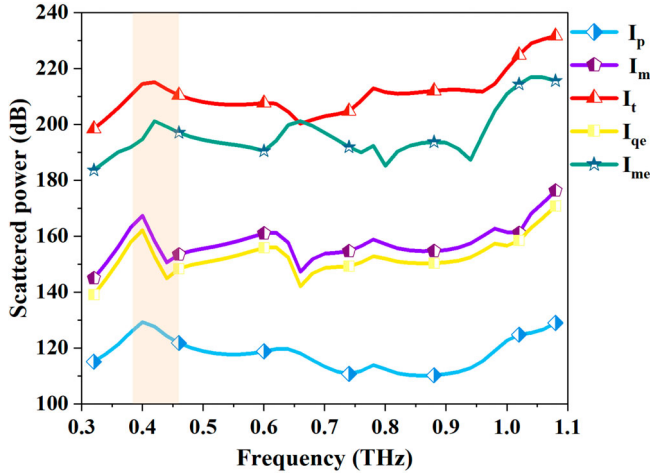


Figure 7. The near-field scattering power of the EIT behavior in different multipoles.

3. The transformation from EIT to EIA

Based on the classic three-atomic energy levels, four-atomic energy levels which are suitable for the twin-peak EIT could be an analogy, as is available in Figure 8. With the participation of the probe light, some atoms transit from the ground state $|1\rangle$ to the excitation level $|2\rangle$ while the other moves along $|1\rangle \rightarrow |2\rangle \rightarrow |3\rangle \rightarrow |2\rangle$, two separate transmission valleys appear on the transmission spectrum. After the addition of the pump light, another channel appears: $|1\rangle \rightarrow |2\rangle \rightarrow |4\rangle \rightarrow |2\rangle$, where the transition between the energy state $|1\rangle$ and the $|3\rangle$ is dipole forbidden. Overall, this level scheme allows for three different excitation pathways: the direct transition $|1\rangle \rightarrow |2\rangle$, the indirect one $|1\rangle \rightarrow |2\rangle \rightarrow |3\rangle \rightarrow |2\rangle$ and $|1\rangle \rightarrow |2\rangle \rightarrow |4\rangle \rightarrow |2\rangle$. When these three methods are excited to the opposite phase of the electrons on the $|2\rangle$, destructive interference will appear, and the absorption on the wide spectrum will be inhibited. On the contrary, opening up a narrow transmission transparent window. The first excitation pathway will interfere with the second and the third excitation pathways respectively, with the coherent elimination occurring at $|2\rangle$ [40]. In this work, the channels $|1\rangle \rightarrow |2\rangle$ are occupied by VR, and S represents the process of $|3\rangle \rightarrow |2\rangle$ while AR occupies $|4\rangle \rightarrow |2\rangle$.

4. The appearance of the EIA phenomenon

As is displayed in Figure 9(a), the curve of EIA enjoys two peaks at 0.429 THz and 0.678 THz, which is the location of an original transparent window of EIT, with one peak arriving at 0.607 and another reaching 0.904. Besides, the highest one among the three zero-absorptions is not more than 0.14. The transmission and reflection curves of the two VO₂ resonators are exhibited in Figure 9(b) when the VO₂ is working in the metallic state, it can be found from which that what contributes to the formation of EIA may be credited to its high reflection which increases the loss of dark mode. EIA comes from the critical coupling theory, when VO₂ in a metallic state participates in resonance, original EIT serves as

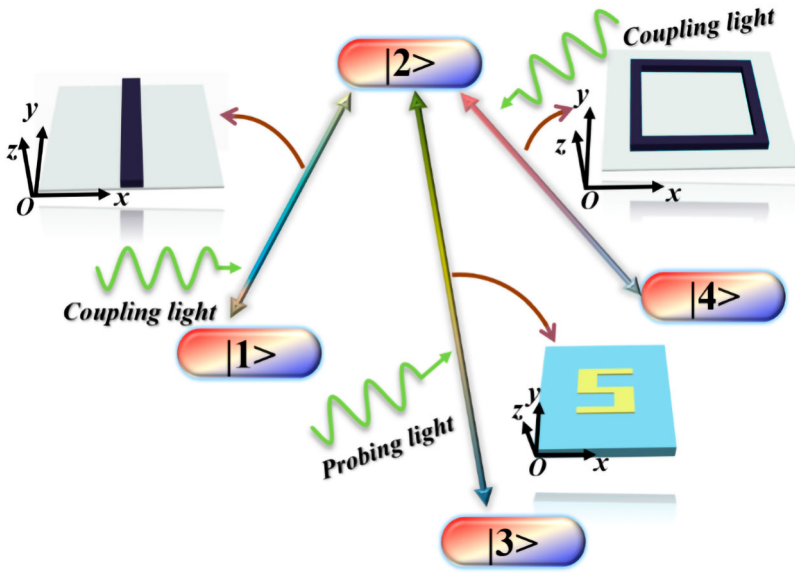


Figure 8. The comparison between the coupling mechanism between the classical atomic system and three given resonators.

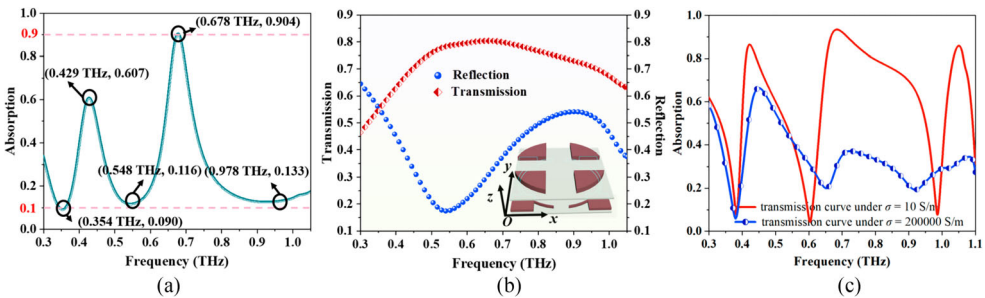


Figure 9. (a) The absorption curve simulated when $\sigma = 200,000$ S/m. (b) The transmission and absorption curves of the two resonators made of VO_2 when $\sigma = 200,000$ S/m. (c) The transmission curve when $\sigma = 10$ S/m and $200,000$ S/m separately.

resonance. The critical coupling in a classic two resonators system means that energy transferred between the bright and dark that takes balance with the energy dissipated by the whole system, while in this work it should be the energy between the three oscillators takes balance with the energy dissipated by the whole system. In this place, VO_2 acts as a perfect reflector, and it can be seen that the incident wave transmitted difficulty in the investigated frequency region compared with the original result, as can be seen in Figure 8(c). The VO_2 structure in a metallic state dramatically depresses the THz transmission [21,62,63]. Compared with Figure 2(d,e), the resonance of two resonators made of VO_2 wider the metal state can be seen (Figure 10).

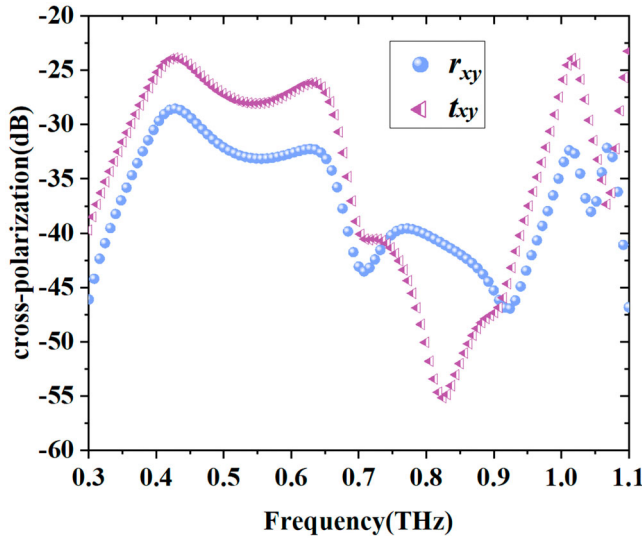


Figure 10. Reflected coefficients and transmission coefficients of the cross-polarization r_{xy} and t_{xy} respectively.

Absorption A can be described by two frequency-dependent parameters including reflectivity R and transmissivity T , as displayed below:

$$A = 1 - R - T - |r_{xy}|^2 - |t_{xy}|^2 \quad (12)$$

where R stands for the reflection coefficient and T represents the transmission coefficient, while r_{xy} and t_{xy} refer to the cross-polarization of reflection and transmission, respectively. Values of r_{xy} and t_{xy} are too small that can be ignored.

As has been reported by metamaterials, ideal impedance matching between free space and target objects provides a powerful approach to total absorption. Therefore, the impedance matching principle is used to understand the physical mechanism behind the absorption phenomenon.

Utilizing S-parameter inversion, the normalized equivalent impedance Z_r of the proposed MS is calculated by Equation (5)

$$Z_r = \sqrt{\frac{(1 + S_{11})^2 - S_{21}^2}{(1 - S_{11})^2 - S_{21}^2}} \quad (13)$$

When the imaginary and real components of Z_r are close to 1 and 0, respectively, EIA will be achieved. The imaginary and real components are shown by the red and blue curves in Figure 11's Z_r of the absorption curve. It is evident that at the two sites that lead to the absorption peaks, the imaginary part of Z_r is floating about 0 and the actual component of Z_r is floating around 1. This indicates the model and free space exhibit an effective impedance matching, allowing more electromagnetic waves to enter the structure and escape without being reflected. The reason why the real part does not exactly equal 1 and the imaginary part does not just equal 0 at the two absorption peaks could be some faint reflection still exists.

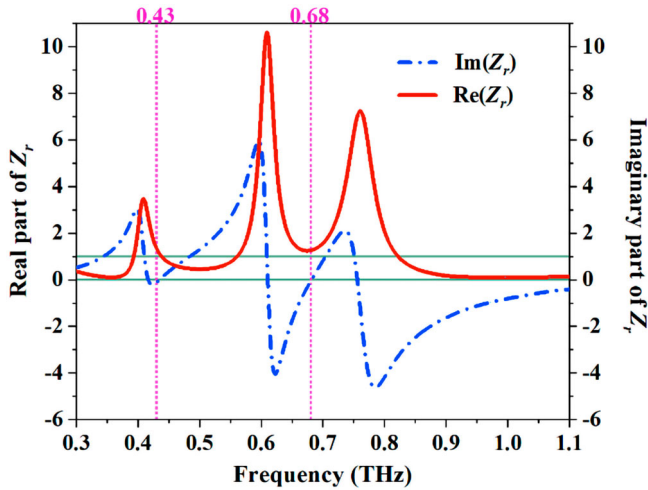


Figure 11. The imaginary and real parts of Z_r .

Figure 12 shows the currents or displacement currents corresponding to resonators with $\sigma = 200,000 \text{ S/m}$. When operating at 0.422 THz, the surface current of SSR turns stronger and reverse compared with the resonant curve stimulated alone displayed in Figure 4, at which time, the displacement current of VR and SR becomes too weak to be considered in comparison with the intensity in the two VO_2 resonators. In this case, the displacement current on ORB is almost concentrated on the four squares made of VO_2 , flowing in the negative direction of the y -axis. On FFB, displacement current forms several local circulation, with the strongest parts of which are located at the edges of each sector. When turning to 0.684 THz, the phenomenon is similar to that at 0.422 THz while enjoying a relatively weaker displacement current of ORB and a comparatively stronger displacement current on FFB. It can be analyzed from Figure 12(d) that the displacement current on ORB starts to weaken at the four edges of squares and that of FFB gets an overall enhancement, accompanied by the direction of both that keeps invariant. This shows that even though the double peaks of EIA are inseparable from these two resonators, which one of the two resonators plays a stronger role in the specific peak is different. To add, it should be pointed out that even if the displacement currents on VR and SR are much weaker than the two resonators made of VO_2 , they are still stronger than those of EIT.

5. Parameter discussion

5.1. Discussion of EIT parameters

To furtherly observe how parameters affect the properties of MS, the influences of L on both EIT windows are considered in Figure 13. The left transmission window appears blueshift and the peak drops slowly from 0.88 to 0.85, with the continuous growth of L ranging from $80 \mu\text{m}$ to $93 \mu\text{m}$. The left zero-transmission point also emerges blueshift, crossing 0.074 THz in the wake of its peak. It can be inferred from Figure 13 that in a certain range, the transmission peak decreases slowly when two zero-transmission points get closer. What can be also analyzed from the figure is that the change in the size of resonator SSR thanks to the

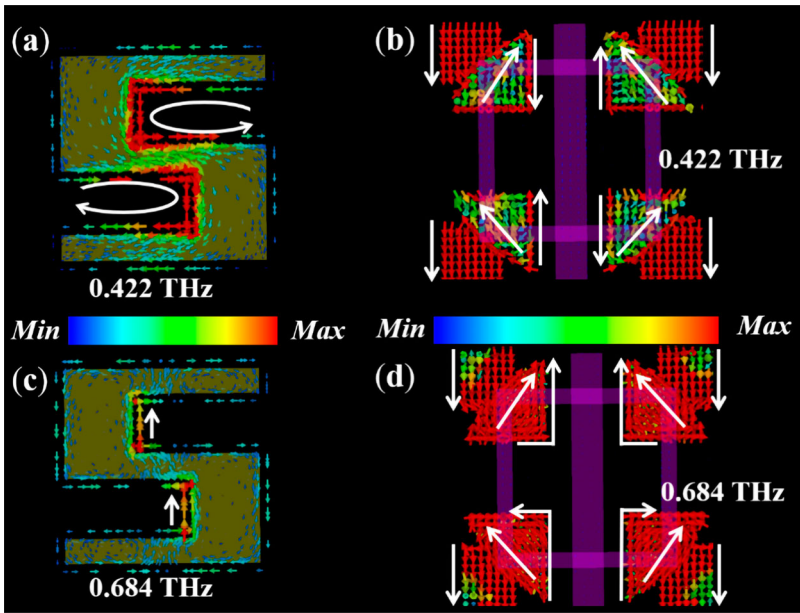


Figure 12. (a) and (c) Different current distribution of SSR on the left peak value at 0.422 THz and the right peak value at 0.684 THz when $\sigma = 200,000$ S/m, (b) and (d) Under two absorption windows the respective displacement current distribution of the four resonators made of the dielectric at 0.422 and 0.684 THz.

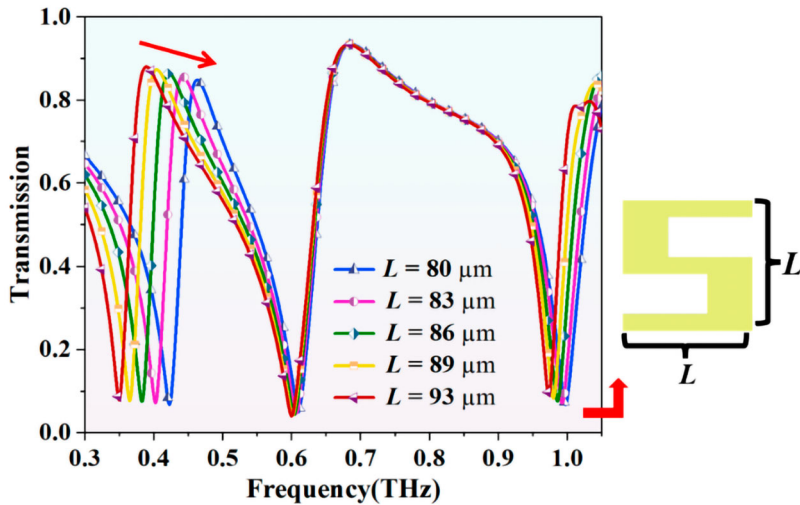


Figure 13. Transmission curves under different values of L .

far distance between a little effect on the second transmission window once again proves it is not involved in the resonance of VR and SR. To enable the frequency to align as much as possible while the peak value is not too low, $L = 86 \mu\text{m}$ is adopted finally.

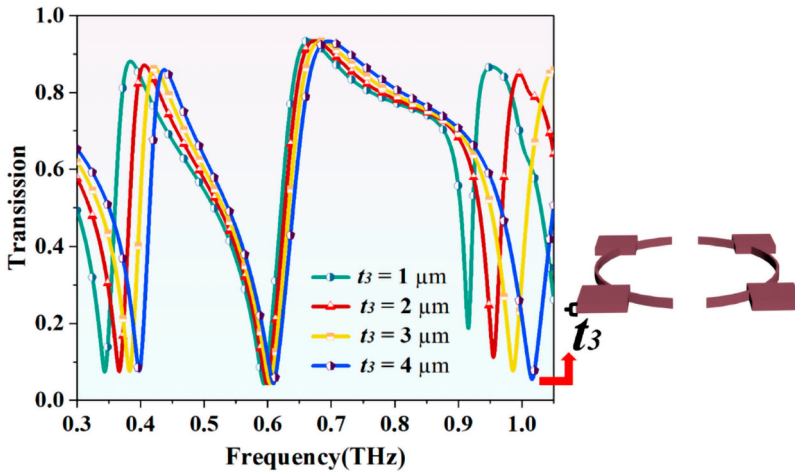


Figure 14. Transmission curves with different values of thicknesses of t_3 .

t_3 stands for the thickness of ORB, the adjustment of which can influence both windows is presented in Figure 14. When t_3 shifts from $1 \mu\text{m}$ to $4 \mu\text{m}$, the transmission window holistically blueshifts, reflected in the left zero-transmission point moving from 0.344 to 0.4. Without any doubt, the peak drops a little from 0.88 to 0.86 because of the increase in vertical coupling distance. Moreover, the zero-transmission point on the right hand reduces sharply from 0.19 to 0.06 under the condition of almost no change of the value of the right peak, the growing distance between SSR and SR that makes a weaker impact on the second peak may account for it.

The impacts of changes in incident angles θ on transmission and absorption are reflected in Figure 15. It is obvious that even change in a little angle, the EIT phenomenon will be deeply destroyed, with the second transmission window rifting two valleys at about 0.76 THz and 0.88 THz respectively, which will deepen when the value of θ grows up. As is clear, the model is sensitive to the change of incident angle θ , even a little change that will deeply impact the transmission curve.

Figure 16 exhibits how polarization angles ϕ plays a role in transmission curves. Accompanied by the increase in ϕ , three zero-transmission points of the transmission curve grow up to 0.4, and a rift valley appears in the middle of the transmission window on the right. With the ϕ exceeding 30° , the EIT phenomenon gradually disappears, and the value of the zero-transmission points of the EIT increases too much, explaining that polarization is not sensitive at a small angle. As the ϕ increases, each resonator cannot be well excited by electromagnetic waves like before, and as a result of which, the coupling will worsen.

5.2. Discussion of EIA parameters

It can be easily captured from Figure 17 that the right absorption peak has almost no changes at all, with the left peak of which growing from 0.58 to 0.66 while the curve of the other is stable. As the value of the left peak increases, the left transparent window gradually narrows and the first zero-transmission point turns blueshift, a similar phenomenon could also be found in the transmission curves. The reason accounting for this phenomenon is

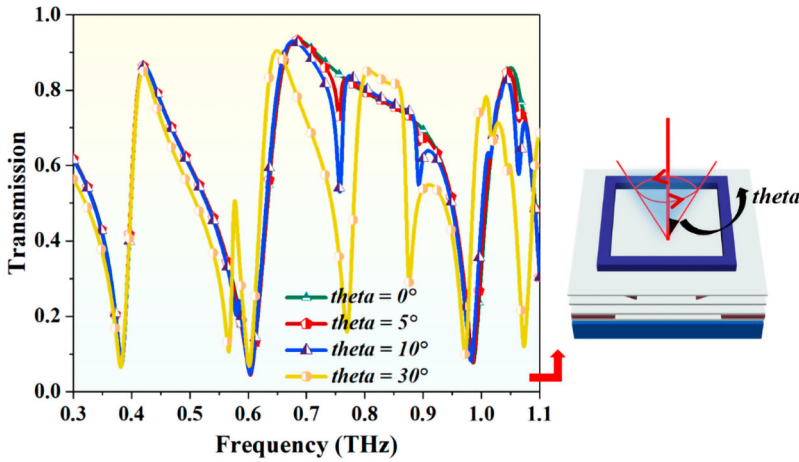


Figure 15. Transmission curves plotted under different incident angle θ .

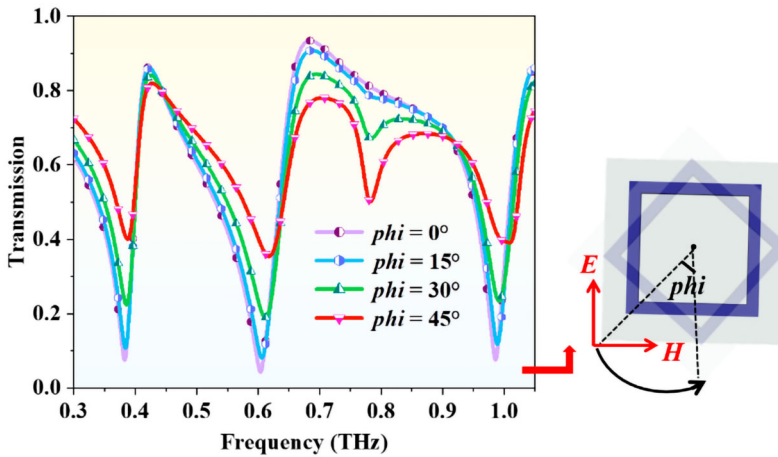


Figure 16. Transmission curves when polarization angle ϕ are different.

that the SSR does not participate in the formation of the latter absorption peak, as a result of which changing in its parameters do not affect the latter absorption window.

The absorption curves at different thicknesses t_3 have been displayed in Figure 18. The growth of t_3 brings in higher absorption on the right, from 0.72 to 0.91, accompanied by the left peak rising from 0.59 to 0.66, which shows a blueshift. The reduction of the left absorption peak is caused by the rise of its corresponding transmission peak, yet what impacts the right may be the increased losses of SR brought by the ORB. It is obvious that as the left peak gets slightly higher, the right peak gets lower relatively quickly when t_3 rises from $1 \mu\text{m}$ to $3 \mu\text{m}$. To enable EIT and EIA to reach the indicators at the same time, $t_3 = 3 \mu\text{m}$ is chosen.

Accompanied by θ rising from 0° to 10° , both absorption windows show nearly no change, for the no change of the frequency points and peaks of EIT, as is shown in Figure 19. When θ exceeds 10° , the second absorption peak of EIA gradually split into two peaks, corresponding to the newly split peaks of EIT. The basic invariance of the left

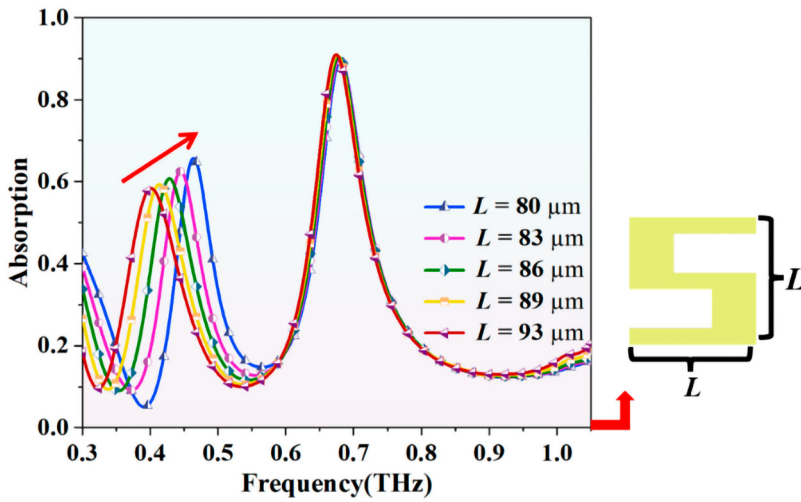


Figure 17. Absorption curves under different values of L .

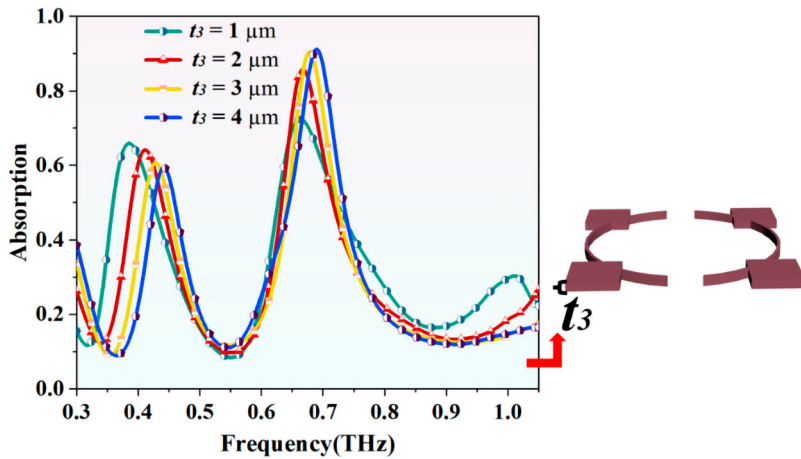


Figure 18. Absorption curves at different thicknesses t_3 .

winger indicates that the transmission curve in small angles is insensitive to the θ , while the insensitivity of this model to incident angle θ is again demonstrated in EIA curves.

Figure 20 shows how polarization angles ϕ work in absorption curves. With the increase of ϕ , two absorption peaks drop rapidly by more than 0.2 and 0.3 respectively, forming a valley around 0.7 THz. When ϕ exceeds 30° , the EIA phenomenon will gradually disappear, the twin peaks of EIA all downing over 0.22, explaining that polarization is not sensitive at a small angle. Corresponding to EIT, the worsened coupling may explain the broken absorption curve.

The details of the physical mechanism of EIT and EIA behavior and the slow-light effect of the EIT behaviors can be seen in the supplementary document.

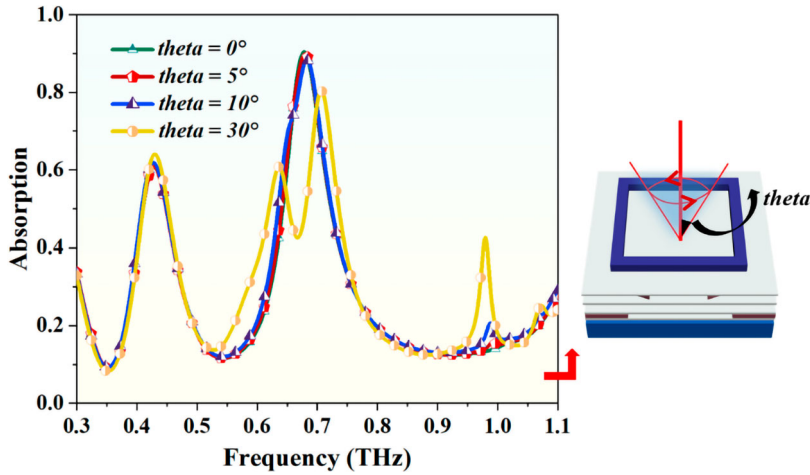


Figure 19. Absorption curves under different incident angles θ .

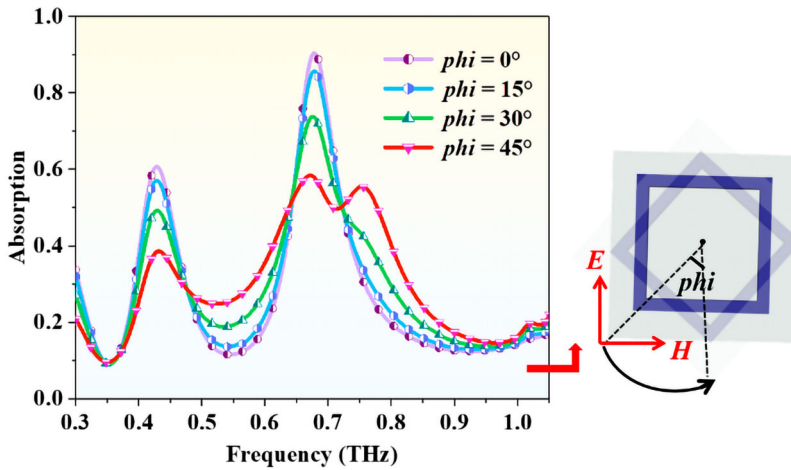


Figure 20. Absorption curves under different polarization angle ϕ .

6. Conclusion

To conclude, with the incidence of linear polarization waves, the adjustable transformation from twin-peak EIT to twin-peak EIA can be achieved by adjusting the conductivity of VO_2 . Calculated in the THz band, when setting VO_2 in a dielectric state, the two transmission peaks reach up to 86.4% at 0.421 THz and 93.4% at 0.684 THz, respectively. After switching to a metallic state, there are two absorption peaks in the original transmission window, each of which reaches 60.7% and 90.4%. Double EIT transparent window spans from 0.382 THz to 0.986 THz with the two maximum t_{GD} reaching 7.55 and 4.54 ps. The theory of classic atomic energy levels is analogized for qualitative analysis of this model while the adoption of the circuit model for quantitative analysis determines the effectiveness and consistency of the simulation result. At the same time, the current and the displacement current distribution further prove the correctness of the model. This design provides a promising solution for

the realization of the adjustable multi-frequency EIT to EIA, which can be applied to antenna fields, or otherwise multi-functional devices.

Disclosure statement

No potential conflict of interest was reported by the author(s).

References

- [1] Marangos JP. Electromagnetically induced transparency. *J Mod Opt.* 1998;45(3):471–503. DOI:10.1080/09500349808231909
- [2] Fleischhauer M, Imamoglu A, Marangos JP. Electromagnetically induced transparency: optics in coherent media. *Rev Mod Phys.* 2005;77(2):633. DOI:10.1103/RevModPhys.77.633
- [3] Zhang S, Genov DA, Wang Y, et al. Plasmon-induced transparency in metamaterials. *Phys Rev Lett* 2008;101(4):047401. DOI:10.1103/PhysRevLett.101.047401
- [4] Singh R, Al-Naib I, Chowdhury DR, et al. Probing the transition from an uncoupled to a strong near-field coupled regime between bright and dark mode resonators in metasurfaces. *Appl Phys Lett.* 2014;105(8):081108. DOI:10.1063/1.4893726
- [5] Yahiaoui R, Burrow JA, Mekonen SM, et al. Electromagnetically induced transparency control in terahertz metasurfaces based on bright-bright mode coupling. *Phys Rev B.* 2018;97(15):155403. DOI:10.1103/PhysRevB.97.155403
- [6] Han S, Cong LQ, Lin H, et al. Tunable electromagnetically induced transparency in coupled three-dimensional split-ring-resonator metamaterials. *Sci Rep.* 2016;6(1):20801. DOI:10.1038/srep20801
- [7] Yin X, Feng T, Yip SP, et al. Tailoring electromagnetically induced transparency for terahertz metamaterials: from diatomic to triatomic structural molecules. *Appl Phys Lett.* 2013;103(2):021115. DOI:10.1063/1.4813553
- [8] Lim WX, Manjappa M, Pitchappa P. Shaping high-Q planar fano resonant metamaterials toward futuristic technologies. *Adv Opt Mater.* 2018;6(19):1800502. DOI:10.1002/adom.201800502
- [9] Srivastava YK, Manjappa M, Krishnamoorthy HNS, et al. Accessing the high-Q dark plasmonic fano resonances in superconductor metasurfaces. *Adv Opt Mater.* 2016;4(11):1875–1881. DOI:10.1002/adom.201600354
- [10] Tan TCW, Plum E, Singh R. Lattice enhanced Fano resonances from bound states in the continuum metasurfaces. *Adv Opt Mater.* 2020;8(6):1901572. DOI:10.1002/adom.201901572
- [11] Han S, Cong LQ, Gao F, et al. Observation of Fano resonance and classical analog of electromagnetically induced transparency in toroidal metamaterials. *Ann Phys.* 2016;528(5):352–357. DOI:10.1002/andp.201600016
- [12] Al-Naib I, Singh R, Rockstuhl C, et al. Excitation of a high-Q subradiant resonance mode in mirrored single-gap asymmetric split ring resonator terahertz metamaterials. *Appl Phys Lett.* 2012;101(7):071108. DOI:10.1063/1.4745790
- [13] Yang Y, Kravchenko II, Briggs DP, et al. All-dielectric metasurface analogue of electromagnetically induced transparency. *Nat Commun.* 2014;5(1):1–7. DOI:10.1038/ncomms6753
- [14] Han S, Pitchappa P, Wang WH, et al. Extended bound states in the continuum with symmetry-broken terahertz dielectric metasurfaces. *Adv Opt Mater.* 2021;9(7):2002001. DOI:10.1002/adom.202002001
- [15] Yao G, Ling F, Yue J, et al. Dynamically electrically tunable broadband absorber based on graphene analog of electromagnetically induced transparency. *IEEE Photon J.* 2015;8(1):1–8. DOI:10.1109/JPHOT.2015.2513210
- [16] Da L, Li JS. Dual-band terahertz switch based on EIT/Fano effect. *Opt Commun.* 2020;472:125862. DOI:10.1016/j.optcom.2020.125862
- [17] Zhang XQ, Li Q, Cao W, et al. Polarization-independent plasmon-induced transparency in a fourfold symmetric terahertz metamaterial. *IEEE J Sel Top Quant Electr.* 2012;19(1):8400707–8400707. DOI:10.1109/JSTQE.2012.2200656

- [18] Lezama A, Barreiro S, Akulshin AM. Electromagnetically induced absorption. *Phys Rev A*. 1999;59(6):4732. DOI:[10.1103/PhysRevA.59.4732](https://doi.org/10.1103/PhysRevA.59.4732)
- [19] Taubert R, Hentschel M, Källste J, et al. Classical analog of electromagnetically induced absorption in plasmonics. *Nano Lett* 2012;12(3):1367. DOI:[10.1021/nl2039748](https://doi.org/10.1021/nl2039748)
- [20] Tassin P, Zhang L, Zhao R, et al. Electromagnetically induced transparency and absorption in metamaterials: the radiating two-oscillator model and its experimental confirmation. *Phys Rev Lett* 2012;109(18):187401. DOI:[10.1103/PhysRevLett.109.187401](https://doi.org/10.1103/PhysRevLett.109.187401)
- [21] Zhang X, Xu N, Qu K. Electromagnetically induced absorption in a three-resonator metasurface system. *Sci Rep*. 2015;5(1):1–9. DOI:[10.1038/srep10737](https://doi.org/10.1038/srep10737)
- [22] Chae BG, Youn DH, Kim HT, et al. Fabrication and electrical properties of pure VO₂ phase films fabrication and electrical properties of pure VO₂ phase films, arXiv preprint cond-mat. 0311616; 2003.
- [23] Liu H, Wang ZH, Li L, et al. Vanadium dioxide-assisted broadband tunable terahertz metamaterial absorber. *Sci Rep*. 2019;9(1):1–10. DOI:[10.1038/s41598-019-42293-9](https://doi.org/10.1038/s41598-019-42293-9)
- [24] Casu EA, Muller AA, Cavalieri M, et al. A reconfigurable inductor based on vanadium dioxide insulator-to-metal transition. *IEEE Microw Compon Lett*. 2018;28(9):795–797. DOI:[10.1109/LMWC.2018.2854961](https://doi.org/10.1109/LMWC.2018.2854961)
- [25] Song ZY, Zhang JH. Achieving broadband absorption and polarization conversion with a vanadium dioxide metasurface in the same terahertz frequencies. *Opt Express*. 2020;28(8):12487–12497. DOI:[10.1364/OE.391066](https://doi.org/10.1364/OE.391066)
- [26] Markov P, Appavoo K, Haglund RF, et al. Hybrid Si-VO₂-Au optical modulator based on near-field plasmonic coupling. *Opt Express*. 2015;23(5):6878–6887. DOI:[10.1364/OE.23.006878](https://doi.org/10.1364/OE.23.006878)
- [27] Antunez EE, Salazar-Kuri U, Estevez JO, et al. Porous silicon-VO₂ based hybrids as possible optical temperature sensor: wavelength-dependent optical switching from visible to near-infrared range. *J Appl Phys*. 2015;118(13):1345039. DOI:[10.1063/1.4932023](https://doi.org/10.1063/1.4932023)
- [28] He XJ, Wang JM, Tian XH, et al. Dual-spectral plasmon electromagnetically induced transparency in planar metamaterials based on bright–dark coupling. *Opt Commun*. 2013;291:371–375. DOI:[10.1016/j.optcom.2012.11.019](https://doi.org/10.1016/j.optcom.2012.11.019)
- [29] Manjappa MA, Solanki A, Kumar A, et al. Solution-processed lead iodide for ultrafast all-optical switching of terahertz photonic devices. *Adv Mater*. 2019;31(32):1901455. DOI:[10.1002/adma.201901455](https://doi.org/10.1002/adma.201901455)
- [30] Motoki T, Ikeda S, Honda G, et al. Dramatic effects of chlorine addition on expanding synthesis conditions for fluorine-free metal–organic decomposition YBa₂Cu₃O_y films. *Appl Phys Express*. 2017;10(2):023102. DOI:[10.7567/APEX.10.023102](https://doi.org/10.7567/APEX.10.023102)
- [31] Manjappa M, Chiam SY, Cong LQ, et al. Tailoring the slow light behavior in terahertz metasurfaces. *Appl Phys Lett*. 2015;106(18):181101. DOI:[10.1063/1.4919531](https://doi.org/10.1063/1.4919531)
- [32] Sariaeddeen H, Alouini MS, Al-Naffouri TY. An overview of signal processing techniques for terahertz communications. *Proc IEEE*. 2021;109(10):1628–1665. DOI:[10.1109/JPROC.2021.3100811](https://doi.org/10.1109/JPROC.2021.3100811)
- [33] Gao ED, Li HJ, Liu ZM, et al. Terahertz multifunction switch and optical storage based on triple plasmon-induced transparency on a single-layer patterned graphene metasurface. *Opt Express*. 2020;28(26):412061. DOI:[10.1364/OE.412061](https://doi.org/10.1364/OE.412061)
- [34] Sen S, Ahmed K. Design of terahertz spectroscopy based optical sensor for chemical detection. *SN Appl Sci*. 2019;1(10):1–8. DOI:[10.1007/s42452-019-1247-0](https://doi.org/10.1007/s42452-019-1247-0)
- [35] Tan TC, Srivastava YK, Ako RT, et al. Active control of nanodielectric-induced THz quasi-BIC in flexible metasurfaces: a platform for modulation and sensing. *Adv Mater*. 2021;33(27):2100836. DOI:[10.1002/adma.202100836](https://doi.org/10.1002/adma.202100836)
- [36] Iwaszczuk K, Strikwerda AC, Fan KB, et al. Flexible metamaterial absorbers for stealth applications at terahertz frequencies. *Opt Express*. 2012;20(1):635–643. DOI:[10.1364/OE.20.000635](https://doi.org/10.1364/OE.20.000635)
- [37] Zhang S, Park YS, Li JS, et al. Negative refractive index in chiral metamaterials. *Phys Rev Lett* 2009;102(2):023901. DOI:[10.1103/PhysRevLett.102.023901](https://doi.org/10.1103/PhysRevLett.102.023901)
- [38] Casse BDF, Lu WT, Huang YJ, et al. Super-resolution imaging using a three-dimensional metamaterials nanolens. *Appl Phys Lett*. 2010;96(2):023114. DOI:[10.1063/1.3291677](https://doi.org/10.1063/1.3291677)
- [39] Singh R, Zheludev N. Superconductor photonics. *Nat Photon*. 2014;8(9):679–680. DOI:[10.1038/nphoton.2014.206](https://doi.org/10.1038/nphoton.2014.206)

- [40] Erçağlar V, Hajian H, Özbay E. VO₂–graphene-integrated hBN-based metasurface for bi-tunable phonon-induced transparency and nearly perfect resonant absorption. *J Phys D Appl Phys*. 2021;54(24):245101. DOI:10.1088/1361-6463/abecb2
- [41] Osgouei AK, Hajian H, Serebryannikov AE, et al. Hybrid indium tin oxide-Au metamaterial as a multiband bi-functional light absorber in the visible and near-infrared ranges. *J Phys D Appl Phys*. 2021;54(27):275102. DOI:10.1088/1361-6463/abf579
- [42] Zhong M, Jiang XT, Zhu XL, et al. Design and fabrication of a single metal layer tunable metamaterial absorber in THz range. *Opt Laser Technol*. 2020;125:106023. DOI:10.1016/j.optlastec.2019.106023
- [43] Shen NH, Massaouti M, Gokkavas M, et al. Optically implemented broadband blueshift switch in the terahertz regime. *Phys Rev Lett* 2011;106(3):037403. DOI:10.1103/PhysRevLett.106.037403
- [44] Brown WD, Grannemann WW. CV characteristics of metal-titanium dioxide-silicon capacitors. *Solid State Electr*. 1978;21(6):837–846. DOI:10.1016/0038-1101(78)90308-8
- [45] Liu ZM, Li Y, Zhang J, et al. Design and fabrication of a tunable infrared metamaterial absorber based on VO₂ films. *J Phys D Appl Phys*. 2017;50(38):385104. DOI:10.1088/1361-6463/aa8338
- [46] Luo ZF, Wu ZM, Xu XD, et al. Study of nanocrystalline VO₂ thin films prepared by magnetron sputtering and post-oxidation. *Chin Phys B*. 2010;19(10):106103. DOI:10.1088/1674-1056/19/10/106103
- [47] Nag J, Payzant EA, More KL, et al. Enhanced performance of room-temperature-grown epitaxial thin films of vanadium dioxide. *Appl Phys Lett*. 2011;98(25):251916. DOI:10.1063/1.3600333
- [48] Kocer H, Butun S, Banar B, et al. Thermal tuning of infrared resonant absorbers based on hybrid gold-VO₂ nanostructures. *Appl Phys Lett*. 2015;106(16):161104. DOI:10.1063/1.4918938
- [49] Singh R, Al-Naib I, Chowdhury DR, et al. Probing the transition from an uncoupled to a strong near-field coupled regime between bright and dark mode resonators in metasurfaces. *Appl Phys Lett*. 2014;105(8):081108. DOI:10.1063/1.4893726
- [50] Yang Y, Kravchenko II, Briggs D, et al. Dielectric metasurface analogue of electromagnetically induced transparency. *CLEO*. 2015;2015. DOI:10.1364/CLEO_QELS.2015.FW4C.7
- [51] Sun YZ, Gao CJ, Qu J, et al. Circularly polarized manipulations with VO₂-doped dielectric electromagnetically induced transparency and absorption. *Ann Phys*. 2022;534(6):2200130. DOI:10.1002/andp.202200130
- [52] Li H, Xu W, Cui Q, et al. Theoretical design of a reconfigurable broadband integrated metamaterial terahertz device. *Opt Express*. 2020;28(26):40060–40074. DOI:10.1364/OE.414961
- [53] Němec H, Kadlec K, Kadlec F, et al. Resonant magnetic response of TiO₂ microspheres at terahertz frequencies. *Appl Phys Lett*. 2012;100(6):061117. DOI:10.1063/1.3683540
- [54] Wang Y, Leng Y, Wang L, et al. Broadband tunable electromagnetically induced transparency analogue metamaterials based on graphene in terahertz band. *Appl Phys Express*. 2018;11(6):062001. DOI:10.7567/apex.11.062001
- [55] Niu LF, Zhang JB, Fu YH, et al. Fano resonance in dual-disk ring plasmonic nanostructures. *Opt Express*. 2011;19(23):22974–22981. DOI:10.1364/OE.19.022974
- [56] Miroshnichenko AE, Flach S, Kivshar YS. Fano resonances in nanoscale structures. *Rev Mod Phys*. 2010;82:2257–2298. DOI:10.1103/RevModPhys.82.2257
- [57] Luk'yanchuk B, Zheludev NI, Maier SA, et al. The Fano resonance in plasmonic nanostructures and metamaterials. *Nat Mater*. 2010;9(9):707–715. DOI:10.1038/nmat2810
- [58] Peng B, Özdemir SK, Chen W, et al. What is and what is not electromagnetically induced transparency in whispering-gallery microcavities. *Nat Commun*. 2014;5(1):509–5082. DOI:10.1038/ncomms6082
- [59] Wang S, Zhao T, Yu S, et al. High-performance nano-sensing and slow-light applications based on tunable multiple Fano resonances and EIT-like effects in coupled plasmonic resonator system. *IEEE Access*. 2020;8:40599–40611. DOI:10.1109/ACCESS.2020.2974491
- [60] Gao CJ, Zhang D, Zhang HF. Simultaneously achieving circular-to-linear polarization conversion and electromagnetically induced transparency by utilizing a metasurface. *Ann Phys*. 2022;534(4):2100578. DOI:10.1002/andp.202100578
- [61] Lv Y, Zhu DD, Yin Y J, et al. Broadband electromagnetically induced transparency to broadband electromagnetically induced absorption conversion with silicon based on.

- [62] Liu C, Xu Y, Liu H, et al. Switchable metamaterial with terahertz buffering and absorbing performance. *IEEE Photon J.* 2021;13(5):1–8. DOI:[10.1109/JPHOT.2021.3107533](https://doi.org/10.1109/JPHOT.2021.3107533)
- [63] Matsumori K, Fujimura R, Retsch M. Coupling strength and total damping govern electromagnetically induced absorption in coupled plasmonic systems. *Adv Photon Res.* 2023: 2200211. DOI:[10.1002/adpr.202200211](https://doi.org/10.1002/adpr.202200211)